

MAGNETIC FIELDS IN HIGH-MASS INFRARED DARK CLOUDS

T. PILLAI^{1,2}, J. KAUFFMANN^{1,2}, J. C. TAN³, P. F. GOLDSMITH⁴, S. J. CAREY⁵, AND K. M. MENTEN²

¹ California Institute of Technology, Cahill Center for Astronomy and Astrophysics, Pasadena, CA 91125, USA; tpillai.astro@gmail.com

² Max Planck Institut für Radioastronomie, Auf dem Hügel 69, D-53121 Bonn, Germany

³ University of Florida, Gainesville, FL 32611, USA

⁴ Jet Propulsion Laboratory, California Institute of Technology, 4800 Oak Grove Drive, Pasadena, CA 91109, USA

⁵ Spitzer Science Center, California Institute of Technology, 1200 East California Boulevard, MC 314-6, Pasadena, CA 91125, USA

Received 2014 August 23; accepted 2014 October 27; published 2015 January 16

ABSTRACT

High-mass stars are cosmic engines known to dominate the energetics in the Milky Way and other galaxies. However, their formation is still not well understood. Massive, cold, dense clouds, often appearing as infrared dark clouds (IRDCs), are the nurseries of massive stars. No measurements of magnetic fields in IRDCs in a state prior to the onset of high-mass star formation (HMSF) have previously been available, and prevailing HMSF theories do not consider strong magnetic fields. Here, we report observations of magnetic fields in two of the most massive IRDCs in the Milky Way. We show that IRDCs G11.11–0.12 and G0.253+0.016 are strongly magnetized and that the strong magnetic field is as important as turbulence and gravity for HMSF. The main dense filament in G11.11–0.12 is perpendicular to the magnetic field, while the lower density filament merging onto the main filament is parallel to the magnetic field. The implied magnetic field is strong enough to suppress fragmentation sufficiently to allow HMSF. Other mechanisms reducing fragmentation, such as the entrapment of heating from young stars via high-mass surface densities, are not required to facilitate HMSF.

Key words: ISM: clouds – ISM: magnetic fields – polarization – stars: formation

1. INTRODUCTION

High-mass (O- and B-type, $M > 8 M_{\odot}$) stars live wild and die young. In spite of their short lifetime, they dominate the energetics over a wide range of scales from the interstellar medium of the Milky Way to that of high-redshift galaxies. While these stars play a crucial role in the cosmos, there are several aspects of their formation that are still not well understood (Tan et al. 2014).

The birth sites of massive stars, cold dense cores, can often appear as infrared dark clouds (IRDCs), silhouetted against the diffuse MIR emission of the Galactic plane (Perault et al. 1996; Carey et al. 1998). The evolution of these natal clouds is expected to be governed by some combination of gravity, turbulence, and magnetic fields, but the relative importance of these effects has been difficult to determine. While the first two factors can be explored relatively easily, the signatures of magnetic fields are much harder to detect. No estimate of magnetic field strengths in IRDCs in a state prior to the onset of high-mass star formation (HMSF) have previously been available (Tan et al. 2014).

The IRDCs G11.11–0.12 and G0.253+0.016 are among the first discovered and darkest shadows in the galactic plane (Carey et al. 1998). G11.11–0.12 is at a distance of 3.6 kpc, has a length ~ 30 pc, a mass of $10^5 M_{\odot}$, and is known to host a single site with a high-mass protostar (Pillai et al. 2006b; Henning et al. 2010; Kainulainen et al. 2013). G0.253+0.016, with a length of 9 pc and $10^5 M_{\odot}$, lies in the Galactic center region at a distance of ≈ 8.4 kpc; it is one of the most massive and dense clouds in the Galaxy but does not yet host high-mass stars (Lis & Menten 1998; Longmore et al. 2012; Kauffmann et al. 2013b). Largely unperturbed by active HMSF, these two clouds thus provide ideal sites for studying the magnetic field at the very beginning of HMSF.

Polarized thermal dust emission can trace the magnetic field in molecular clouds. Dust grains in molecular clouds become aligned with their major axes preferentially oriented perpendicular to the magnetic field most likely through radiative torques (Lazarian 2007). This mechanism of grain alignment requires asymmetrical radiation fields, and thus for the IRDCs being studied here (with no internal sources) the alignment would be most efficient on the surfaces of the clouds. Thermal continuum emission from such aligned grains is polarized. The field direction can be traced by rotating the polarization vectors by 90° (Crutcher 2012). Here we present the first such analysis available for prominent high-mass IRDCs. These data constrain for the first time the magnetic field properties during the assembly of massive dense clouds.

2. OBSERVATIONS AND DATA REDUCTION

We analyze archival calibrated polarization data obtained for G11.11–0.12. Specifically, we used data for high-mass prestellar cores from the SCUPOL catalog, which is a compilation of calibrated and reduced $850 \mu\text{m}$ polarization observations made with the James Clerk Maxwell Telescope (JCMT; Matthews et al. 2009). The JCMT project ID for G11.11–0.12 is m03bc32. Only a part of the 30 pc long cloud is covered by the SCUBA polarization observations. The data were sampled on a $10''$ pixel grid and the effective beam width in the map is $20''$. Similarly, we use $350 \mu\text{m}$ archival polarization data from the Caltech Submillimeter Observatory (CSO; Dotson et al. 2010) for G0.253+0.016 which have a spatial resolution of $20''$.

3. RESULTS

The images presented in Figures 1 and 2 summarize the results of the archival polarization observations with the polarization vectors rotated by 90° to represent B -vectors, i.e., the orientation

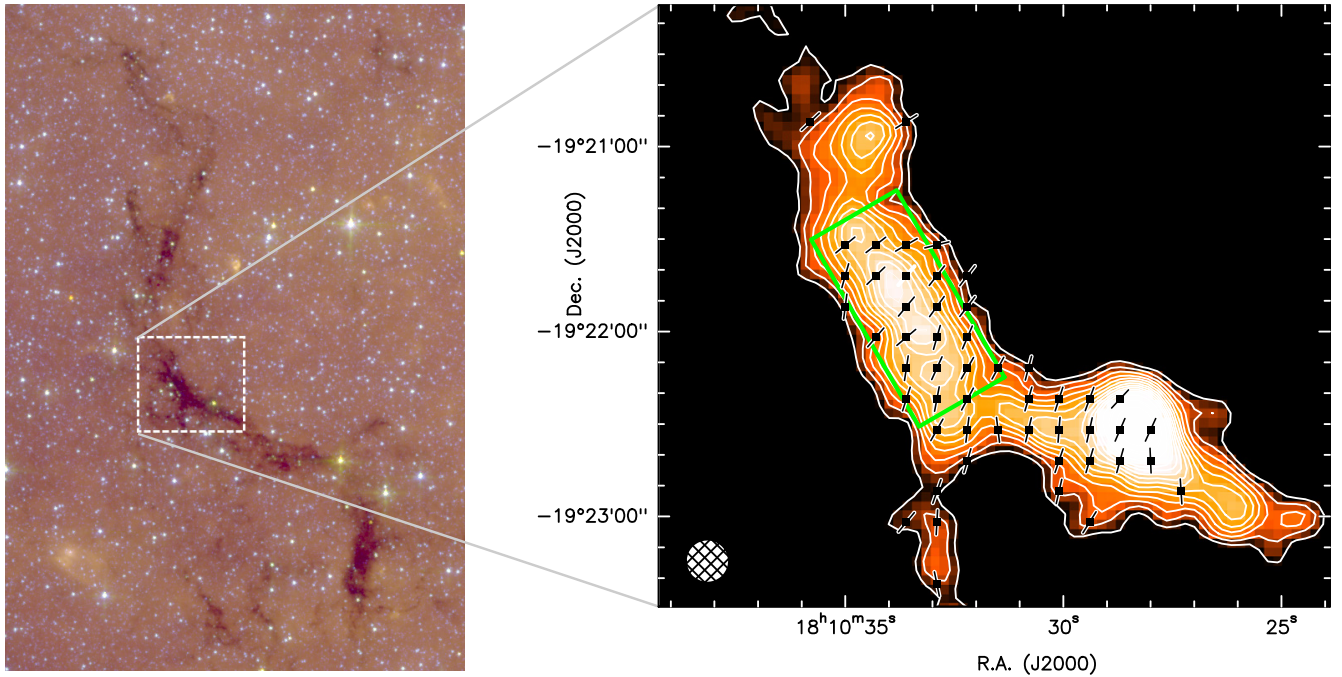


Figure 1. Polarization data for the G11.11–0.12 IRDC. The left panel presents an infrared overview image obtained using *Spitzer Space Telescope* data (at 3.6, 5.8, 8.0 μm). The box indicates the area highlighted in the right panel. The right panel shows magnetic field vectors obtained by rotating polarization vectors by 90° . The green box outlines the region for which the magnetic field strength is determined. The background and contours show SCUBA 850 μm dust intensities. Contours are drawn in steps of $0.05 \text{ Jy beam}^{-1}$, starting at 0.1 Jy beam^{-1} . Polarization data (Matthews et al. 2009) are only shown where (1) the ratio of the polarization level to its uncertainty is ≥ 3 , corresponding to an error in polarization angle $\leq 10^\circ$, and (2) the SCUBA 850 μm dust intensity is greater than 0.1 Jy beam^{-1} . The hatched circle corresponds to the SCUBA 850 μm beam.

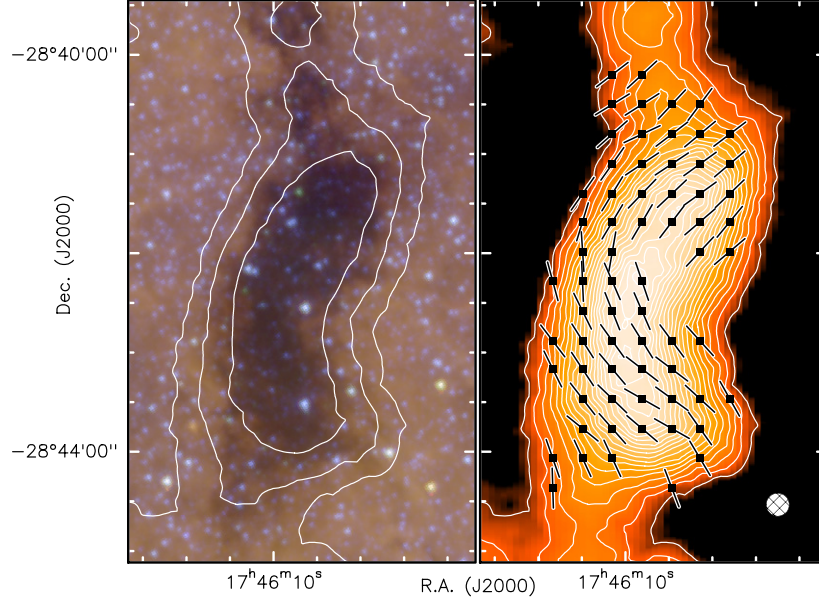


Figure 2. Polarization data for the G0.253+0.016 IRDC. The left panel presents an infrared overview image obtained using *Spitzer Space Telescope* data (at 3.6, 5.8, 8.0 μm). Selected Bolocam 1.1 mm dust intensity (Aguirre et al. 2011; Ginsburg et al. 2013) contours are overlaid. The right panel shows magnetic field vectors obtained by rotating polarization vectors by 90° . The background image and contours give the Bolocam 1.1 mm dust intensity distribution. Contours are drawn in steps of 0.2 Jy beam^{-1} , starting at 0.2 Jy beam^{-1} . Polarization data (Dotson et al. 2010) is only shown where (1) the ratio of the polarization level to its uncertainty is ≥ 3 , corresponding to an error in polarization angle $\leq 10^\circ$, and (2) the 1.1 mm dust intensity is greater than 0.2 Jy beam^{-1} . The hatched circle corresponds to the CSO 1.1 mm beam.

of the magnetic field on the plane of the sky at the location of the polarization vector. The dust continuum emission is shown in colorscale (right panel) with the plane-of-sky component of the B -field (B_{pos}) overlaid. To study the initial conditions before the onset of star formation, we limit our analysis of G11.11–0.12 to

a section of the filament enclosed by the box in Figure 1, which is well detached from the $8 \mu\text{m}$ bright embedded young high-mass star in the western part of the filament (Pillai et al. 2006b; Gómez et al. 2011; Ragan et al. 2014; Wang et al. 2014), while we study the full extent of G0.253+0.016. The mean position

angle (noise-weighted) of the magnetic field for G11.11–0.12, averaged over all the positions shown within the box in Figure 1 is 147° east of north. On the plane of the sky, the angle subtended by the main axis of the cloud (i.e., the spine of the filament) is 30° east of north. Therefore, the magnetic field is mainly perpendicular to the major axis of the filament in G11.11–0.12. The lowest dust intensity contours also reveal a more diffuse elongated structure merging onto the main filament, and it is parallel to the magnetic field. For G0.253+0.016, the magnetic field shows a kinked morphology that correlates well with the structure of the cloud. The magnetic field is remarkably ordered in both clouds, with small angular dispersions $\sigma_\phi \leq 17^\circ$ relative to the mean cloud field (see Section 3.1).

Small angle dispersions suggest very strong fields. Following Chandrasekhar & Fermi (1953), we may assume that local perturbations imposed on the mean field direction, characterized by the standard deviation σ_ϕ of the residual position angles, are caused by random “turbulent” gas motions of one-dimensional velocity dispersion σ_v inside the clouds. Then the plane-of-sky component, B_{pos} , is (Chandrasekhar & Fermi 1953)

$$B_{\text{pos}} = f \sqrt{4\pi\varrho} \frac{\sigma_v}{\sigma_\phi}, \quad (1)$$

where σ_ϕ is measured in radians and ϱ is the mass density of the region in the cloud relevant to the σ_ϕ and σ_v values. We include the correction factor $f = 0.5$, based on studies using synthetic polarization maps generated from numerically simulated clouds (Ostriker et al. 2001; Heitsch et al. 2001) which suggest that for $\sigma_\phi \leq 25^\circ$ Equation (1) is uncertain by a factor of two.

3.1. Methods

To apply the Chandrasekhar–Fermi method for estimates of the magnetic field strength, we have to infer how much the magnetic field is disturbed by the “turbulent” gas motions inside the cloud and thus determine σ_ϕ . To do this, we must essentially separate the magnetic field on the plane of the sky, \mathbf{B}_{pos} into an undisturbed underlying field \mathbf{B}_0 on which disturbances \mathbf{B}_t are superimposed such that $\mathbf{B} = \mathbf{B}_0 + \mathbf{B}_t$. For example, in Equation (1), the disturbances \mathbf{B}_t are characterized via the dispersion of polarization angles σ_ϕ relative to the direction of the underlying field. Separating the observed polarization vectors into the components \mathbf{B}_0 and \mathbf{B}_t is the subject of the current subsection.

3.1.1. Method I: Spatial Filtering of the Underlying Field

As mentioned earlier, the magnetic field vectors in G11.11–0.12 (specifically within the highlighted box in Figure 1) are roughly aligned along an axis running southeast to northwest, which is predominantly perpendicular to the main filament. The dispersion among these angles shall therefore yield σ_ϕ . In G0.253+0.016, the global field structure is, however, more complex and the underlying field cannot be approximated as having a spatially constant orientation throughout the cloud.

A more sophisticated approach is needed to determine a model of the underlying field that allows for large-scale variations inside the cloud. A straightforward way of estimating the underlying field is to model the field as a distance-weighted mean of the neighboring positions. We thus subtract the average polarization angle in the neighborhood of every independent pixel in the map (the spatial-filter method). In G11.11–0.12, no changes in the mean field direction are evident. Thus, we use filtering scales as large as the size of the box indicated in

Figure 1. In G0.253+0.016, the filter should be smaller than the spatial scale on which the well-defined background field changes. Inspection of Figure 2 shows that the field changes its orientation on an angular scale $\lesssim 200''$. The mean-field removal should thus be done on a scale significantly smaller than this. In practice, we use a maximum filter scale of $200''/4 = 50''$, which is significantly larger than the telescope beam. Using data points that were pre-selected by the spatial filter, we then calculate the residual polarization angle as

$$\phi_{i,\text{res}} = \phi_i - \frac{\sum_{j=1}^N w_{i,j} \cdot \phi_j}{\sum_{j=1}^N w_{i,j}}, \quad (2)$$

where $w_{i,j} = \sqrt{1/S_{i,j}}$ is the weighting function, and $S_{i,j}$ is the separation between the pixels. We calculate the dispersion in residual angles $\sigma_{\phi,\text{obs}}$ as the standard deviation in $\phi_{i,\text{res}}$. Even for a perfectly polarized source, noise in the data introduces a non-zero dispersion. We then correct the dispersion for this measurement uncertainty (δ_ϕ) by subtracting it from the estimated dispersion, i.e., the corrected dispersion $\sigma_\phi = \sqrt{\sigma_{\phi,\text{obs}}^2 - \delta_\phi^2}$ (see Equation (3) of Hildebrand et al. 2009). We find σ_ϕ to be $16:2$ for G11.11–0.12. This is an upper limit to σ_ϕ : filter scales smaller than the size of the box in Figure 1 yield lower values. In G0.253+0.016, a maximum filter scale of $200''/4 = 50''$ yields $\sigma_\phi = 9:3$. Smaller filter scales that are still resolved by the beam yield values as low as $8:4$, while increasing the filter size to $200''/3 = 67''$ gives $\sigma_\phi = 11:2$. Thus, we adopt $\sigma_\phi = 9:3$ for G0.253+0.016, with an uncertainty of 20% at most. Results using Method I are reported in Table 1.

3.1.2. Method II: Structure Function Analysis

Given the larger number of polarization vectors in G0.253+0.016, we also explore a recent structure function method (Hildebrand et al. 2009; Houde et al. 2009) to test the robustness of our results. This method relies on the two-point correlation (angular dispersion) function, which has the form

$$\xi(\ell) \equiv 1 - \langle \cos[\Delta\Phi(\ell)] \rangle \simeq \frac{1}{N} \frac{\langle B_t^2 \rangle}{\langle B_0^2 \rangle} \left(1 - e^{-\frac{\ell^2}{2(\delta^2 + 2W^2)}} \right) + a_2' \ell^2, \quad (3)$$

where $\Delta\Phi(\ell)$ is the difference in the polarization angle measured at two positions separated by a distance ℓ , B_t and B_0 are the turbulent and large-scale ordered components, respectively, δ is the turbulent correlation length, W is the beam radius, and a_2' is the slope of the “higher-order effects.” This relation holds when ℓ is less than a few times W . The factor N corrects for the integration along the line of sight and is defined as the number of independent turbulent cells probed by observations. Following Houde et al. (2009), if Δ' is the depth along the line of sight, then $N = (\delta^2 + 2W^2)\Delta'/\sqrt{2\pi}\delta^3$. The magnetic field is then found to have the form (Houde et al. 2009)

$$B_0 = \sqrt{4\pi\varrho} \sigma_v \left(\frac{\langle B_t^2 \rangle}{\langle B_0^2 \rangle} \right)^{-1/2}. \quad (4)$$

Equations (1) and (4) imply $\langle B_t^2 \rangle / \langle B_0^2 \rangle \sim [\sigma_\phi / f]^2$. The fit parameters are $\langle B_t^2 \rangle / \langle B_0^2 \rangle$, δ , and a_2' , while W and Δ' are assumed. The fit quality is assessed as the reduced χ^2 by comparing the observed two-point correlation function for binned separations ℓ_i , $\xi_{\text{obs}}(\ell_i)$ to those modeled by

Table 1
Physical Properties and Magnetic Field Parameters

Source	Distance (pc)	$\sigma_{\text{obs}}(v)$ (km s ⁻¹)	Mass (M_{\odot})	$\langle N_{\text{H}_2} \rangle$ (10 ²³ cm ⁻²)	Density (10 ⁴ cm ⁻³)	σ_{ϕ} (deg)	B_{tot} (μG)	\mathcal{M}_{A}	$\frac{(M/\Phi_B)}{(M/\Phi_B)_{\text{cr}}}$
G11.11–0.12 ^a	3600	0.9 ± 0.1	549 ₂₇₅ ¹⁰⁹⁸	0.4 _{0.2} ^{0.8}	3 ₁ ⁶	<16.2 ± 1.6	>267 ± 26 ₁₆₃ ⁴³⁷	< 0.8 ± 0.1 _{0.5} ^{1.2}	<1.1 ± 0.1 _{0.6} ^{2.1}
G0.253+0.016	8400	6.4 ± 0.4	(2 ₁ ⁴) × 10 ⁵	4 ₂ ⁸	8 ₄ ¹⁶	9.3 ± 0.9 _{7.8} ^{11.2}	5432 ± 525 ₃₃₁₂ ⁸⁹⁰⁸	0.4 ± 0.1 _{0.3} ^{0.7}	0.6 ± 0.1 _{0.3} ^{1.1}

Notes. Gas velocity dispersion ($\sigma_{\text{obs}}(v)$) (Pillai 2006; Kauffmann et al. 2013b), average column density over the same area where B_{pos} is measured ($\langle N_{\text{H}_2} \rangle$), H₂ density (Density) (Pillai et al. 2006a; Longmore et al. 2012), standard deviation of the residual polarization angles (σ_{ϕ}), total magnetic field (B_{tot}), Alfvén Mach number (\mathcal{M}_{A}), and mass-to-flux parameter $(M/\Phi_B)/(M/\Phi_B)_{\text{cr}}$. Note that we use a molecular weight per hydrogen molecule of 2.8 to convert from mass to particle density (Kauffmann et al. 2008). There are two distinct sources of errors in our calculations: statistical and systematic. A ± sign is adopted to show the statistical uncertainty determined from a Gaussian error propagation. Since our systematic uncertainties are asymmetric about the central value, we provide the minimum and the maximum value within a 68% central confidence region (i.e., 1σ) about the central estimate. This is represented by the lower and upper bound, respectively, for the relevant parameters.

^a Estimates are made for the material within the bounded box shown in Figure 1.

Equation (3), $\xi(\ell_i)$:

$$\chi_{\text{red}}^2 \equiv \frac{\chi^2}{\nu} = \frac{1}{\nu} \sum_i \left(\frac{\xi_{\text{obs}}(\ell_i) - \xi(\ell_i)}{\sigma(\xi_{\text{obs}}[\ell_i])} \right)^2, \quad (5)$$

where $\sigma(\xi_{\text{obs}}[\ell_i])$ is the uncertainty on $\xi_{\text{obs}}(\ell_i)$ (Equation (B6) of Houde et al. 2009). The number of degrees of freedom, ν , is given by the number of observations used in the fit minus the number of free-fitting parameters.

We find that the goodness of fit is insensitive to a wide range of values of δ when the other two parameters, $\langle B_{\text{r}}^2 \rangle / \langle B_0^2 \rangle$ and a_2' , are left unconstrained. We do, therefore, follow a different approach to constrain δ . In the analysis of Houde et al. (2009), δ describes the spatial scale below which the observed turbulent fluctuations in velocity and magnetic polarization become small (i.e., clouds become “coherent” in the terminology of Goodman et al. 1998). Note that this is an observational property: scales much smaller than the telescope beam cannot be resolved, and so $\delta \gtrsim W$. This conjecture is also consistent with the hierarchical nature of molecular clouds: observed properties are always dominated by the structure on the largest unresolved spatial scale, which is again $\sim W$ in our situation. This implies a total of $N \leq 10$ cells along the line of sight. This is consistent with our previous interferometer observations (Kauffmann et al. 2013b) where we deduce that the cloud has about seven velocity components.

In our fits to the data, we therefore require $\delta \geq W$ as a constraint to the fit. Only the first four data points are fitted to fulfill the constraint that separations $\ell \gg W$ should be excluded (Houde et al. 2009). The parameter a_2' is left unconstrained, while we evaluate χ^2 for a wide range in the parameter $\langle B_{\text{r}}^2 \rangle / \langle B_0^2 \rangle$ (see below). This results in two degrees of freedom ($\nu = 2$). Fits consistent with the data at a confidence level of 90% must then achieve $\chi_{\text{red}}^2 < 2.3$. Allowing δ and a_2' to vary as described above, we find that fixed values of $\langle B_{\text{r}}^2 \rangle / \langle B_0^2 \rangle \leq 0.5$ are consistent with this constraint in χ_{red}^2 . This upper limit on $\langle B_{\text{r}}^2 \rangle / \langle B_0^2 \rangle^{1/2}$ is basically an upper limit on σ_{ϕ}/f . If we maintain our estimate of σ_{ϕ} from Method I, then the result here implies $f \geq 0.23$, instead of $f = 0.5$. Based on this, we will assume an uncertainty of two in Method I associated with Equation (1) where $f = 0.5$ (see Section 3.2).

3.2. Magnetic Field Strength

For our calculations, we utilize the spatial-filter method (Method I) since it is a model-independent approach that can be applied to both clouds.

The density in Equation (1) is derived from prior observations of dust emission. For G11.11–0.12, we use the 850 μm dust emission observations reported in Pillai et al. (2006a) to derive the mass within the bounded box shown in Figure 1. For this, we use the temperature measurement for the same region (Pillai et al. 2006a). We approximate the region within the box as a homogeneous cylinder to estimate an average density. For G0.253+0.016, we adopt the average density determined over the entire cloud (i.e., exactly the same region used in our analysis) from published millimeter dust observations (Longmore et al. 2012). As stated earlier, the alignment mechanism of the dust grains is likely to be most efficient in the outer portions of the cloud, and thus our determination of σ_{ϕ} is probably biased toward these outer regions of the cloud. The above derived average densities for G11.11–0.12 and G0.253+0.016 would not be too different from the densities in these outer regions of the clouds; therefore, these are acceptable estimates of ρ for Equation (1).

The N₂H⁺ emission shows an excellent correlation with dust emission and thus traces the dust throughout the cloud. We derive the velocity dispersion from N₂H⁺ observations for both clouds (Pillai 2006; Kauffmann et al. 2013b). To do this, we spatially integrate all the spectra within the box shown in Figure 1 for G11.11–0.12 and the within the whole cloud shown in Figure 2. for G0.253+0.016.

It is the non-thermal component of the total velocity dispersion that influences the magnetohydrodynamic (MHD) turbulence. The thermal component operates on scales lower than that of the ambipolar diffusion scale and, therefore, would not contribute to the observed dispersion in the field orientation. Therefore, we equate σ_v in Equation (1) with $\sqrt{\Delta v_{\text{obs}}^2 / (8 \ln 2) - k_{\text{B}} T_{\text{g}} / m}$, where Δv_{obs} is the line width observed for the integrated N₂H⁺ line, k_{B} and T_{g} are the Boltzmann constant and the gas temperature, respectively, and m is the mass of a N₂H⁺ molecule. We assume that σ_v is almost uniform throughout the starless clouds we are studying; thus, the value of σ_v derived here is a reasonably good estimate of the level of velocity dispersion responsible for the observed σ_{ϕ} . Table 1 lists the values we use in Equation (1) to determine the plane of the sky magnetic field strengths, B_{pos} for G11.11–0.12 and G0.253+0.016. Furthermore, Table 1 gives the resulting total magnetic field strength for these clouds, $B_{\text{tot}} = 1.3 B_{\text{pos}}$, by using an average field geometry (Crutcher et al. 2004).

Table 1 contains statistical uncertainty estimates obtained via regular Gaussian error propagation of noise. In addition, we also consider the impact of systematic uncertainties. In our analysis,

we assume that σ_v is dominated by its statistical uncertainties only, while we assume that mass, N_{H_2} and ϱ is uncertain by a factor of two, while σ_ϕ is either an upper limit (for G11.11–0.12) or uncertain by a factor of 1.2 (for G0.253+0.016). In addition, we assume that the factor f in Equation (1) has an uncertainty of two (see Section 3.1.2). Equation (1) essentially means that we must consider a product of properties with true values T_i that are scaled by error factors r_i . If we consider, for example, a two factor observable, $T_{\text{obs}} = T_1 \cdot T_2$, then a value of $T_{\text{obs}} = r_1 T_1 \cdot r_2 T_2$ is within its range of uncertainty. Given an uncertainty by a factor of a_i , r_i can vary in the range of $1/a_i \leq r_i \leq a_i$. For our analysis, we consider the logarithm of the observed product, $\log(T_{\text{obs}}) = \log(T_1) + \log(T_2) + \log(r_1) + \log(r_2)$. We assume that the errors $\log(r_i)$ have a flat probability distribution within the range limited by $\pm \log(a_i)$ and are zero for $|\log(r_i)| > \log(a_i)$ (i.e., we adopt a top-hat function). The joint probability distribution of $\log(r_1) + \log(r_2)$ is then calculated by convolving the distributions for the individual $\log(r_i)$. A simple transformation back to the linear space allows us to use the joint probability distribution for $\log(r_1) + \log(r_2)$ to represent the probability distribution of $r_1 \cdot r_2$. We report the resulting uncertainties at the 68% confidence level, corresponding to the classical $\pm 1\sigma$ limit. Without any loss of generality, this approach can be expanded to include an arbitrary number of factors $r_i T_i$. In the current example, $B_{\text{pos}} \propto T_1 T_2 T_3 T_4 = f \varrho^{1/2} \sigma_v \sigma_\phi^{-1}$, where $a_1 = 2$, $a_2 = 2^{1/2}$, and $a_3 \sim 1$ for both clouds. For G0.235+0.016 $a_4 = 1.2$, and for G11.11–0.12 $a_4 = 1$, but the upper limit for σ_ϕ for this cloud is tracked through the quantities derived using σ_ϕ .

3.3. Turbulence, Magnetic Field, and Gravity

To assess the importance of turbulence with respect to the magnetic field, we calculate the Alfvén Mach number that can be expressed as

$$\mathcal{M}_A = \sqrt{3} \sigma_v / v_A \quad (6)$$

(see Table 1), where $v_A = B_{\text{tot}} / \sqrt{4\pi\varrho}$ is the Alfvén speed and $B_{\text{tot}} = 1.3 B_{\text{pos}}$ converts the projected plane-of-sky component to the total magnetic field for an average field geometry (Crutcher et al. 2004). Substitution of Equation (1) reveals that, except for numerical constants, $\mathcal{M}_A \propto \sigma_\phi$. The systematic uncertainty in the Alfvén Mach number is thus identical to the small uncertainty in σ_ϕ .

Can self-gravity overcome magnetic forces to initiate collapse in high-mass IRDCs? The balance is governed by the mass-to-flux ratio M/Φ_B , where the magnetic flux $\Phi_B = \pi \langle B \rangle R^2$ is derived from the mean magnetic field and the radius of the cloud cross-section perpendicular to the magnetic field. The ratio has a critical value (Nakano & Nakamura 1978) $(M/\Phi_B)_{\text{cr}} = 1/(2\pi G^{1/2})$, where G is the gravitational constant. Provided $(M/\Phi_B) < (M/\Phi_B)_{\text{cr}}$, a cloud will not collapse due to self-gravity, even if compressed to higher densities, unless M/Φ_B increases. We find (McKee & Ostriker 2007)

$$\frac{(M/\Phi_B)}{(M/\Phi_B)_{\text{cr}}} = 0.76 \left(\frac{\langle N_{\text{H}_2} \rangle}{10^{23} \text{ cm}^{-2}} \right) \left(\frac{B_{\text{tot}}}{1000 \mu\text{G}} \right)^{-1} \quad (7)$$

(Table 1) when approximating M as $\pi \langle N_{\text{H}_2} \rangle R^2$ times the H_2 mass. We assume $\langle N_{\text{H}_2} \rangle$ to be uncertain by a factor of two, while the uncertainty of B_{tot} comes from Section 3.1.

4. DISCUSSION

These observations have many important consequences. The first implication is that the magnetic field is dynamically important relative to turbulence and, therefore, turbulence is sub-Alfvénic. This is evident from the highly ordered field structure observed in both G11.11–0.12 and G0.253+0.016 that is only slightly perturbed by turbulence. Analyses of synthetic dust polarization maps generated from turbulent three-dimensional MHD simulations also demonstrate that sub-Alfvénic models show strongly correlated field lines as opposed to a very complex structure in super-Alfvénic models (Falceta-Gonçalves et al. 2008). We find Alfvén Mach numbers $\mathcal{M}_A \leq 1.2$ given our systematic errors and formal uncertainties. This also implies that simulations of MHD turbulence with $\mathcal{M}_A \gg 1$ should not apply to HMSF.

The second consequence is that magnetic fields have a significant—and possibly dominant—role in shaping the evolution of clouds toward gravitational collapse. This follows from upper limits $(M/\Phi_B)/(M/\Phi_B)_{\text{cr}} \leq 2.1$ including all uncertainties, with most likely values of $(M/\Phi_B)/(M/\Phi_B)_{\text{cr}} \lesssim 1$. These fields may dramatically slow down collapse due to self-gravity. The forces due to magnetic fields can certainly not be neglected in studies of high-mass IRDC evolution.

Myers (2009) find that local clouds often form hub–filament systems. Young clusters form within dense elongated hubs and lower density filaments converge onto such hubs. Such networks have been observed in other IRDCs as well (Busquet et al. 2013; Peretto et al. 2013). Near-infrared polarization observations that trace magnetic fields in low extinction envelopes of such filaments have shown that the magnetic field on even larger scales may be perpendicular to the dense hub (Chapman et al. 2011; Palmeirim et al. 2013; Busquet et al. 2013; Li et al. 2014). The lower extinction filament in the south of G11.11–0.12 that is merging onto the main dense filament (see Figure 1) appears to be consistent with a hub–filament system. While the main dense filament is perpendicular to the magnetic field, the low column density filament is parallel to the magnetic field. Therefore, the magnetic field may funnel gas into the main filament. Millimeter polarization maps with higher resolution and sensitivity together with information on the velocity distribution are needed to explore this scenario. Fiege et al. (2004) compared the dust continuum data for G11.11–0.12 (shown in Figure 1) to two different magnetic models of self-gravitating, pressure-truncated filaments that are either toroidal or poloidal. The observations presented here rule out a poloidal field. However, they also do not prove the existence of a toroidal field: the observed field lines might coil around the filament, but they might as well be relatively straight on spatial scales larger than the filament and permeate the filament at a random angle.

In G0.253+0.016, the cloud morphology as well as the large-scale field morphology resemble an arched structure opening to the west. Such a morphology might be naively expected when the cloud is shocked due to the impact of material approaching from the west. The presence of multiple velocity components, as well as the existence of spatially extended SiO emission expected in shocks, does indeed support such a scenario for G0.253+0.016 (Lis & Menten 1998; Kauffmann et al. 2013b). It is conceivable that the impacting material might have been ejected in a supernova. A collision between two molecular clouds provides another viable explanation. However, there is no unambiguous evidence supporting any specific scenario. We do, therefore, refrain from a detailed discussion of the global cloud and magnetic field morphology.

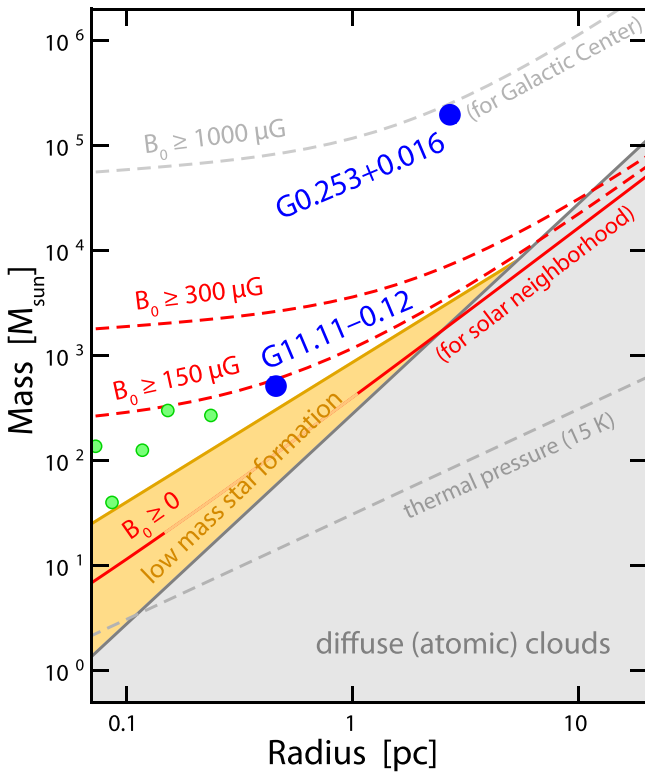


Figure 3. Mass vs. size relationship for molecular cloud stability. The solid red line gives the maximum mass for which an unmagnetized cloud of given radius R would be stable based on typical gas temperatures (≈ 15 K) and velocity dispersion ($\sigma_v \lesssim 0.8 \text{ km s}^{-1} \cdot [R/\text{pc}]^{0.32}$) in the solar neighborhood (Kauffmann et al. 2013a). The mass supported by thermal pressure is indicated by the gray broken line. Diffuse atomic (i.e., non-molecular) clouds, indicated by the gray shading, and many clouds devoid of high-mass star formation, highlighted by yellow shading, do not need magnetic support to be stabilized against collapse. G11.11–0.12 and G0.253+0.016, indicated by blue circles, reside above the red solid line, thus requiring significant magnetic support. Potential high-mass starless cores (Pillai et al. 2011; Tan et al. 2013), indicated by green circles, are also in the mass–size domain requiring significant magnetic support.

The detection of dynamically significant magnetic fields with $(M/\Phi_B) \lesssim (M/\Phi_B)_{\text{cr}}$ in high-mass dense clouds possibly resolves a recent riddle in the study of HMSF sites: many of these clouds are so dense and massive that thermal pressure and random gas motions alone are insufficient to provide significant support against self-gravity (i.e., these clouds have a low virial parameter (Kauffmann et al. 2013a) $\alpha = 5\sigma_v^2 R/[GM]$). This suggested (Pillai et al. 2011; Kauffmann et al. 2013a; Tan et al. 2013) that significant magnetic fields provide additional support. The data presented here provide the first direct evidence for this picture. Figure 3 illustrates this scenario. Typical gas temperatures and velocity dispersions are combined with magnetic fields to provide support against gravitational collapse. A relation (Crutcher 2012) $B = B_0 \cdot (n_{\text{H}_2}/10^4 \text{ cm}^{-3})^{0.65}$ is adopted, where $B_0 \lesssim 150 \mu\text{G}$ is common. Many clouds with pure low-mass star formations can be supported without magnetic fields. However, the more massive HMSF regions need significant magnetic fields, unless they are in an unlikely (Kauffmann et al. 2013a) state of rapid collapse. The observed field strengths for G11.11–0.12 and G0.253+0.016 (see Table 1) are remarkably consistent with the values needed for magnetic support of the two clouds.

These results indicate that strong magnetic fields may play an important role in resolving the “fragmentation problem”

of HMSF (Krumholz & McKee 2008). Collapsing isothermal molecular clouds would fragment into a large number of stars with masses of the order of a solar mass. Increasing the cloud mass would raise the number of stars, but not their mass. High stellar masses, as needed for HMSF, are hard to realize in this situation. “Competitive accretion” models suggest that the stars continue to grow to higher masses by accreting mass from their environment (Bonnell et al. 2001). Some “core accretion” (McKee & Tan 2002) models propose that the gas might heat up so that fragmentation is suppressed and stars of higher mass are formed provided clouds exceed a mass surface density threshold (Krumholz & McKee 2008) $\sim 1 \text{ g cm}^{-2}$. Suppression of fragmentation via strong magnetic fields can provide a natural explanation without requiring a high surface density threshold. While fragmentation (Butler & Tan 2012) and stability (Pillai et al. 2011; Kauffmann et al. 2013a; Tan et al. 2013) studies provide indirect indications for the presence of strong magnetic fields in IRDCs, the observations and analyses presented here provide the first direct evidence. Polarization observations in regions where HMSF has already been initiated reveal that the magnetic field continues to be dynamically significant even after the onset of star formation (Girart et al. 2013; Zhang et al. 2014). Numerical experiments with even supercritical fields demonstrate that the number of fragments is reduced by a factor of ~ 2 when comparing simulations with $(M/\Phi_B)/(M/\Phi_B)_{\text{cr}} \approx 2$ to unmagnetized cases (Commerçon et al. 2011; Myers et al. 2013). Future calculations must still show, however, whether this reduction in fragmentation also results in higher final masses of the stars that are formed.

The inferred strong magnetic fields can imply a slowing down of the star formation process. This is the case when $(M/\Phi_B)/(M/\Phi_B)_{\text{cr}} \leq 1$: the magnetic flux must be reduced significantly before collapse and star formation can occur. Under the influence of strong gravitational forces, ambipolar diffusion in a medium without random gas motions removes the field in a period (McKee & Ostriker 2007) $\tau_{\text{AD}} \approx 1.6 \times 10^6 \text{ yr} \mathcal{X}_{\text{CR}} (n_{\text{H}_2}/10^5 \text{ cm}^{-3})^{-1/2}$, where $\mathcal{X}_{\text{CR}} = \zeta_{\text{CR}}/(3 \times 10^{-17} \text{ s}^{-1})$ captures the impact of the cosmic ray ionization rate ζ_{CR} . This period is long compared to the free-fall timescale, $\tau_{\text{ff}} = 9.8 \times 10^4 \text{ yr} ((n_{\text{H}_2})/10^5 \text{ cm}^{-3})^{-1/2}$. Since $\tau_{\text{AD}} \sim 10 \tau_{\text{ff}}$, one may thus think that star formation in magnetically subcritical clouds is very “slow” compared to the non-magnetic case. However, clouds must only lose part of their magnetic flux to become supercritical (Ciolek & Basu 2000), and random “turbulent” fluctuations reduce τ_{AD} (Fatuzzo & Adams 2002). Even when molecular clouds are supported by significant magnetic pressure, ambipolar diffusion dictates that star formation from a self-gravitating core can occur on a timescale only modestly exceeding τ_{ff} .

We thank P. Redman for his data on G11.11–0.12 and his discussion on the observations. We thank Brenda Matthews for kindly checking the quality of the re-processed SCUPOL data for this source. We thank the referee for a very constructive review of the manuscript that improved the quality of the manuscript. This work was carried out in part at the Jet Propulsion Laboratory, which is operated for NASA by the California Institute of Technology. T.P. and J.K. acknowledge support by the European Commission Seventh Framework Programme (FP7) through grant PIRSES-GA-2012-31578 “EuroCal”. T.P. acknowledges support from the Deutsche Forschungsgemeinschaft (DFG) via the SPP (priority program) 1573 ‘Physics of the ISM’.

Facilities: JCMT (SCUBA, SCUPOL), CSO (Hertz, Bolocam), *Spitzer* (GLIMPSE)

REFERENCES

- Aguirre, J. E., Ginsburg, A. G., Dunham, M. K., et al. 2011, *ApJS*, 192, 4
- Bonnell, I. A., Bate, M. R., Clarke, C. J., & Pringle, J. E. 2001, *MNRAS*, 323, 785
- Busquet, G., Zhang, Q., Palau, A., et al. 2013, *ApJL*, 764, L26
- Butler, M. J., & Tan, J. C. 2012, *ApJ*, 754, 5
- Carey, S. J., Clark, F. O., Egan, M. P., et al. 1998, *ApJ*, 508, 721
- Chandrasekhar, S., & Fermi, E. 1953, *ApJ*, 118, 116
- Chapman, N. L., Goldsmith, P. F., Pineda, J. L., et al. 2011, *ApJ*, 741, 21
- Ciolek, G. E., & Basu, S. 2000, *ApJ*, 529, 925
- Commerçon, B., Hennebelle, P., & Henning, T. 2011, *ApJL*, 742, L9
- Crutcher, R. M. 2012, *ARA&A*, 50, 29
- Crutcher, R. M., Nutter, D. J., Ward-Thompson, D., & Kirk, J. M. 2004, *ApJ*, 600, 279
- Dotson, J. L., Vaillancourt, J. E., Kirby, L., et al. 2010, *ApJS*, 186, 406
- Falceta-Gonçalves, D., Lazarian, A., & Kowal, G. 2008, *ApJ*, 679, 537
- Fatuzzo, M., & Adams, F. C. 2002, *ApJ*, 570, 210
- Fiege, J. D., Johnstone, D., Redman, R. O., & Feldman, P. A. 2004, *ApJ*, 616, 925
- Ginsburg, A., Glenn, J., Rosolowsky, E., et al. 2013, *ApJS*, 208, 14
- Girart, J. M., Frau, P., Zhang, Q., et al. 2013, *ApJ*, 772, 69
- Gómez, L., Wyrowski, F., Pillai, T., Leurini, S., & Menten, K. M. 2011, *A&A*, 529, A161
- Goodman, A. A., Barranco, J. A., Wilner, D. J., & Heyer, M. H. 1998, *ApJ*, 504, 223
- Heitsch, F., Zweibel, E. G., Mac Low, M.-M., Li, P., & Norman, M. L. 2001, *ApJ*, 561, 800
- Henning, T., Linz, H., Krause, O., et al. 2010, *A&A*, 518, L95
- Hildebrand, R. H., Kirby, L., Dotson, J. L., Houde, M., & Vaillancourt, J. E. 2009, *ApJ*, 696, 567
- Houde, M., Vaillancourt, J. E., Hildebrand, R. H., Chitsazzadeh, S., & Kirby, L. 2009, *ApJ*, 706, 1504
- Kainulainen, J., Ragan, S. E., Henning, T., & Stutz, A. 2013, *A&A*, 557, A120
- Kauffmann, J., Bertoldi, F., Bourke, T. L., Evans, N. J., II., & Lee, C. W. 2008, *A&A*, 487, 993
- Kauffmann, J., Pillai, T., & Goldsmith, P. F. 2013a, *ApJ*, 779, 185
- Kauffmann, J., Pillai, T., & Zhang, Q. 2013b, *ApJL*, 765, L35
- Krumholz, M. R., & McKee, C. F. 2008, *Natur*, 451, 1082
- Lazarian, A. 2007, *JQSRT*, 106, 225
- Li, H.-b., Goodman, A., Sridharan, T. K., et al. 2014, arXiv:1404.2024
- Lis, D. C., & Menten, K. M. 1998, *ApJ*, 507, 794
- Longmore, S. N., Rathborne, J., Bastian, N., et al. 2012, *ApJ*, 746, 117
- Matthews, B. C., McPhee, C. A., Fissel, L. M., & Curran, R. L. 2009, *ApJS*, 182, 143
- McKee, C. F., & Ostriker, E. C. 2007, *ARA&A*, 45, 565
- McKee, C. F., & Tan, J. C. 2002, *Natur*, 416, 59
- Myers, A. T., McKee, C. F., Cunningham, A. J., Klein, R. I., & Krumholz, M. R. 2013, *ApJ*, 766, 97
- Myers, P. C. 2009, *ApJ*, 700, 1609
- Nakano, T., & Nakamura, T. 1978, *PASJ*, 30, 671
- Ostriker, E. C., Stone, J. M., & Gammie, C. F. 2001, *ApJ*, 546, 980
- Palmeirim, P., André, P., Kirk, J., et al. 2013, *A&A*, 550, A38
- Perauld, M., Omont, A., Simon, G., et al. 1996, *A&A*, 315, L165
- Peretto, N., Fuller, G. A., Duarte-Cabral, A., et al. 2013, *A&A*, 555, A112
- Pillai, T. 2006, PhD thesis, Max-Planck-Institut für Radioastronomie
- Pillai, T., Kauffmann, J., Wyrowski, F., et al. 2011, *A&A*, 530, A118
- Pillai, T., Wyrowski, F., Carey, S. J., & Menten, K. M. 2006a, *A&A*, 450, 569
- Pillai, T., Wyrowski, F., Menten, K. M., & Krügel, E. 2006b, *A&A*, 447, 929
- Ragan, S. E., Henning, T., & Beuther, H. 2014, arXiv:1411.1911
- Tan, J. C., Beltran, M. T., Caselli, P., et al. 2014, arXiv:1402.0919
- Tan, J. C., Kong, S., Butler, M. J., Caselli, P., & Fontani, F. 2013, *ApJ*, 779, 96
- Wang, K., Zhang, Q., Testi, L., et al. 2014, *MNRAS*, 439, 3275
- Zhang, Q., Qiu, K., Girart, J. M., et al. 2014, *ApJ*, 792, 116